ACS NANO

ARTICLE

Understanding the Elementary Steps in DNA Tile-Based Self-Assembly

Shuoxing Jiang,[†] Fan Hong,[†] Huiyu Hu, Hao Yan,* and Yan Liu*

Center for Molecular Design and Biomimetics at the Biodesign Institute, and School of Molecular Sciences, Arizona State University, Tempe, Arizona 85287, United States

S *Supporting Information*

ABSTRACT: Although many models have been developed to guide the design and implementation of DNA tile-based self-assembly systems with increasing complexity, the fundamental assumptions of the models have not been thoroughly tested. To expand the quantitative understanding of DNA tile-based self-assembly and to test the fundamental assumptions of self-assembly models, we investigated DNA tile attachment to preformed "multi-tile" arrays in real time and obtained the thermodynamic and kinetic parameters of single tile attachment in various sticky end association scenarios. With more sticky ends, tile attachment becomes more thermostable with an approximately linear decrease in the free energy change (more negative). The total binding free energy of sticky ends is partially compromised by a sequence-independent energy penalty when tile attachment forms a constrained configuration: "loop". The minimal loop is a 2 × 2 tetramer (Loop4). The energy penalty of loops of 4, 6, and 8 tiles was analyzed with the independent loop model assuming no interloop tension, which is generalizable to arbitrary tile configurations. More sticky ends also contribute to a faster on-rate under isothermal conditions when nucleation is the rate-limiting step. Incorrect sticky end contributes to neither the thermostability nor the kinetics. The thermodynamic and kinetic parameters of DNA tile attachment elucidated here will contribute to the future improvement and optimization of tile assembly modeling, precise control of experimental conditions, and structural design for error-free self-assembly.

KEYWORDS: *self-assembly, DNA nanotechnology, double-crossover tile, thermodynamics, kinetics*
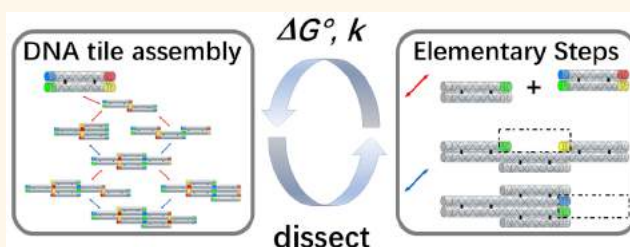
Structural DNA nanotechnology provides a reliable platform for precisely controlling bottom-up self-assembly on the nanometer scale. This is attributed to the remarkable features of DNA molecules including the programmability and specificity of Watson−Crick base pairing, facile and affordable DNA oligosynthesis, and the abundance of DNA manipulation techniques.[1−4] Particularly, the programmability of DNA enables the assembly of basic building units into increasingly complex arbitrary shapes or patterns.[2,3,5,6] The toolbox of DNA tiles has been greatly enriched;[7] motifs including Holliday junction (HJ) tiles,[8,9] double-crossover (DX) tiles,[10,11] paranemic-crossover (PX) tiles,[12,13] multiarm junction tiles,[14−18] single-stranded tiles (SST),[19−21] and others[22−25] have been successfully designed and assembled. Structures built from DNA tiles can serve as templates to arrange inorganic[26,27] or biomolecules[28] for electronic and photonic applications or biomimetic functions. Although a variety of tile motifs have been constructed for homogeneous or heterogeneous tiling, the physicochemical properties of the elementary steps in DNA tile-based self-assembly have not been thoroughly experimentally quantified.

The DX tile is one of the most widely used DNA motifs. It contains two crossovers to interweave strands together[29] and

possesses almost doubled rigidity as compared with a DNA duplex.[30] DX tiles can be engineered to carry, display, and propagate information by encoding single-stranded overhangs, termed sticky ends, with designed matching rules. The sticky ends can be programmed to be orthogonal so that only sticky ends with complementary sequences can bind with each other, while noncomplementary sticky ends are unlikely to stably bind.[31] Moreover, tile attachment through multiple sticky ends is thermodynamically more stable than that with only a single sticky end.[32−34] Periodic assemblies including two-dimensional (2D) lattices[10,32,35] and nanotubes[26,36,37] have been extensively researched as either model systems or nanofabrication templates. Remarkably, DX tile assembly was shown to be Turing universal by abstracting DX tile as "Wang tile".[38,39] This capability has been demonstrated with cellular automaton patterns,[40] DNA Sierpinski triangles,[41] and algorithmic self-assembly systems with self-replication[42,43] or binary counting functions.[44]
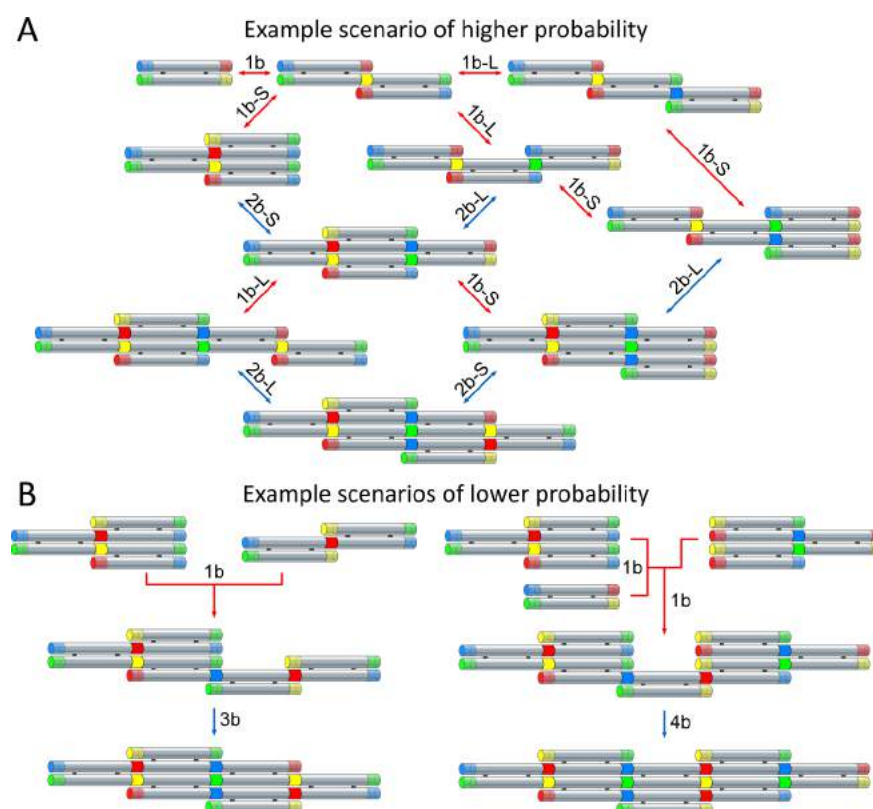
Figure 1. Single tile attachments in the nucleation stage of tile-based self-assembly. (A) Example scenario of the assembly pathway with a higher probability involves binding steps with either one or two sticky ends (1b or 2b). The red arrows indicate less thermodynamically stable binding steps (1b, 1b-S, or 1b-L); the blue arrows indicate more thermodynamically favorable binding steps (2b-S or 2b-L); both arrows repeat in an alternating manner. (B) Example scenarios of the assembly pathway with a lower probability involve the joining of preformed clusters and successive 1b binding steps. The two processes shown here illustrate the formation of transient intermediates with 3b and 4b binding sites, respectively.

The versatility of the DX tile predominantly relies on the thermodynamic and the kinetic control of intertile binding during assembly. A systematic study of tile nucleation and growth will help to improve the robustness and reliability of the DNA tile-based self-assembly system. Many tile assembly models, including the abstract tile assembly model (aTAM), the kinetic tile assembly model (kTAM), *etc.*,[38,45,46] have been developed to enhance the design, prediction, and implementation of tile assemblies. The reversible nature of DNA self-assembly is considered in the kTAM for a more physically realistic understanding of assembly dynamics and assembly error. In the kTAM, an assumption was made that "attachment rates are constant and equal regardless of the number of correct or incorrect bonds for a tile at the binding site". The kinetics of single tile attachment/detachment on a mica surface has been quantified to support this assumption.[33] However, the diffusion rate of tiles on mica is slower than that in solution due to the electrostatic interactions between tiles and the negatively charged surface.[47,48] Therefore, the kinetics of DNA tile assembly in solution might be different from the assumption of kTAM as nucleation rather than tile diffusion becomes the rate-limiting step. Moreover, other key assumptions of the kTAM, including (1) the linear relation between the binding strength and the number of bonds and (2) the effects of incorrect bonds on thermodynamics or kinetics, have not yet been tested in aqueous solution.

To assemble a 2D lattice, the DX tiles attach to one another through sticky ends to form small clusters (nucleation stage); extended structures are assembled by subsequent attachment of single tile or other clusters of tiles (growth stage). In this study, we categorized and defined the scenarios of single tile attachment by the number of correctly formed bonds (*e.g.*, 1b stands for 1-bond attachment, 2b stands for 2-bond attachment and so on) and the arrangement of sticky ends (*e.g.*, L and S stand for "long" or "short" orientation of 2b attachment). An example scenario of the nucleation stage is illustrated in Figure 1A. In this stage, the favorability of a step is mainly determined by its thermostability. Favorable (2b) and less favorable (1b) steps repeat in an alternating manner: a 1b step could induce one or more subsequent 2b steps, driving the system toward the formation of larger complexes. Smaller tile clusters may bind with one another through single or multiple sticky ends to form a larger cluster (Figure 1B), resulting in binding sites with three or four sticky ends. Consequently, a 3b or 4b step will follow. The 3b and 4b steps are relatively rare in the nucleation stage because multiple successive 1b steps must occur sequentially to create such binding sites. The majority of favorable binding steps are 2b steps, either with a "long" orientation (2b-L) or with a "short" orientation (2b-S)[33] (Figures 1A and 2B,C). In the nucleation stage, it is possible that the tile clusters disassemble completely before a nucleus with a critical number of tiles forms. Once a critical nucleus forms, a single less favorable step could create a series of favorable binding sites with multiple sticky ends, thus accelerating growth.[34] The assembly transits into the growth stage.
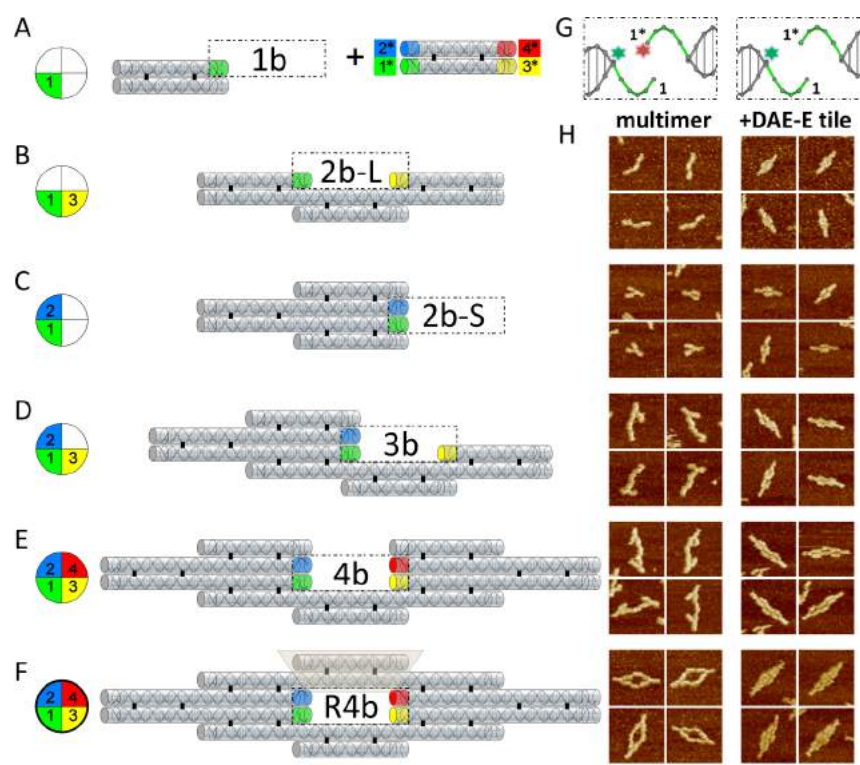
Figure 2. Structural designs for the thermodynamic and kinetic measurements in this study. (A−E) DNA helix model of the flexible multimers. The circles represent the sticky end arrangements of the corresponding binding sites. Each quadrant corresponds to one sticky end pairing. From top to bottom: tile monomer with 1b, trimer with 2b-L, trimer with 2b-S, 5-mer with 3b, 7-mer with 4b, all bind with a tile monomer carrying four sticky ends. Matching colors represent complementary sequences. (F) DNA helix model of the rigid 4b (R4b) multimer. The shaded subunit is the additional tile to encircle the 4b binding site. The bold circle represents the sticky end arrangements of the rigid binding sites. Each quadrant corresponds to one sticky end pairing. The strand sequences are listed in the Supporting Information. (G) Left: For thermodynamic measurement, the pair of green sticky ends were labeled with 6-FAM (green) and TAMRA (red); right: for kinetic measurement, one of the green sticky ends was labeled with 6-FAM. (H) Morphologic observations of the corresponding multimers before and after DAE-E tile attachment by AFM, respectively. Scale bar: 50 nm.

We hypothesize that different geometric arrangements of sticky ends would result in distinct thermodynamic and kinetic properties. Especially for the 2b-L and 2b-S scenarios, the distance between two sticky ends could determine their cooperativity and further affect binding affinity.[49] There could also be energy penalty when a tile must be distorted to fit into the binding site,[38] resulting in constrained product. Moreover, the local binding site that provides either correctly matched sticky ends or a mismatched sticky end may also affect the attachment rates. A quantitative comparison between these scenarios would shed light on the effects of the molecular environment on intermolecular interactions and the corresponding energetics and kinetics.

A DAE-E tile motif[29] (D, double crossover; A, antiparallel; E, even number of helical half-turns between crossovers within the tile and between neighboring tiles) was chosen as the building unit to design a series of binding sites for a monomer DAE-E tile to attach. Tile multimers containing two to eight DAE-E tile subunits were constructed by sealing selected nick points between neighboring tiles (detailed designs in the Supporting Information, section 3). Each tile multimer carried a well-defined binding site with a desired number and geometric arrangement of sticky ends (Figure 2A−F). The sticky ends involved in binding were designed to have unique sequences, while the other ends of the DNA helices were extended with 5 thymines to prevent nonspecific stacking between the tile multimers. The four base pairs at the crossovers were assigned

with a J1 junction sequence so that all the DAE-E tile subunits in the multimers had similar structural distortion induced by Holliday junction isomerization.[50−53] Fluorescent reporters (6-FAM and TAMRA) located at one pair of the sticky ends (SE-1/1*, green) were employed to monitor the local environment of the binding site (Figure 2G). The variation of the 6-FAM intensity was recorded (1) with temperature on a slow temperature ramp to derive the thermodynamic parameters and (2) with time after equimolar mixing under isothermal conditions to derive the kinetic parameters. We observed that (1) the binding free energy is linearly correlated with the number of bonds; (2) an energy penalty must be overcome when tile is attached by two or more bonds; (3) the on-rate of tile attachment depends on the local steric effects of the binding site; (4) mismatched sticky ends neither contribute to a significant energy benefit nor bring any energy penalty. We attributed the energy penalty to the formation of a constrained configuration, termed "loop", by multivalent tile attachment. A single loop comprises tiles that are in series attached into a ring. The free energy changes of all the binding scenarios in this study can be described as a linear combination of sequence-dependent bond strength and sequence-independent loop penalty assuming no interloop tension. The model is termed the independent loop model (ILM).
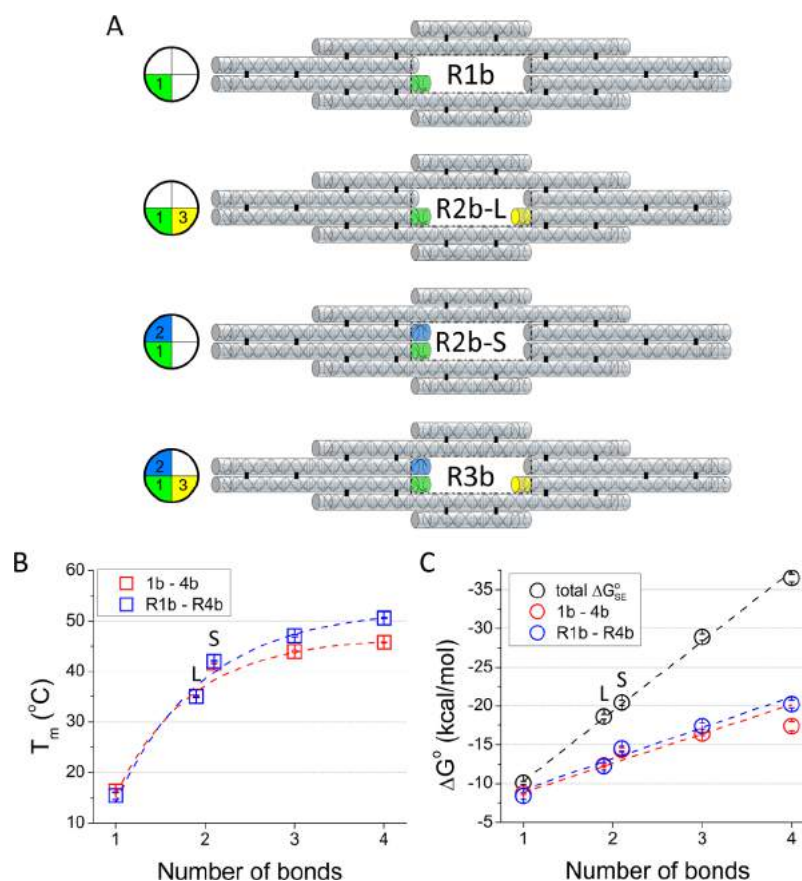
Figure 3. (A) Structural designs of additional rigid binding scenarios. DNA helix model of rigid 1b-3b (R1b-R3b) multimers. (B,C) Melting temperature (T_m) and standard free energy change ($\Delta G°$) of single tile attachment to multimers with an increasing number of bonds. (B) Values of T_m for the flexible (1b-4b) and rigid (R1b-R4b) binding scenarios through variable numbers of sticky ends. Both 2b-L, 2b-S and R2b-L, R2b-S scenarios were shifted horizontally for better comparison. (C) Values of $\Delta G°$ for the flexible (1b-4b) and rigid (R1b-R4b) binding scenarios through variable numbers of sticky ends. The difference between the sum of $\Delta G°_{SE}$ and the corresponding $\Delta G°$ suggests the existence of energy penalty in tile attachment.

RESULTS AND DISCUSSION

Characterization of Multimer Formation and Single Tile Attachment Using AFM. The morphologies of multimers before and after tile attachment were characterized with atomic force microscopy (AFM) (Figure 2H). All of the multimers were formed as designed and could bind to a single tile to produce the corresponding product. The observed morphologies might result from the slightly distorted DX tile,[54] electrostatic repulsion between DNA helical backbones,[55] and also the structural dynamics[56] of the DNA nanostructures that freeze upon deposition on the mica surface.

Taking 2b-S trimer as an example, a gap was observed between the two arms carrying the sticky ends due to the lack of local crossovers between the two arms to fix their relative orientations. Although two reciprocal crossovers exist between the two central helices, they are at least five helical turns (~17–18 nm) away from the sticky ends. The spatial positions of the two sticky ends were not adjacent to each other as shown in the scheme (Figure 2C and Figure S27). The actual distance was amplified by the bending of DNA central helices around the middle crossover. The 2b-L trimer may be equally distorted as the 2b-S trimer from the "ideal" configuration (Figure 2B). The 3D bending of the central helix in the 2b-L trimer had become flattened in the 2D projection when it was deposited onto the mica to maximize the contact with the substrate. In all cases, the flexibility and dynamic motions of the multimers decreased

significantly with the multivalent binding of a newly attached tile (Figure 2H; additional AFM images in Figures S26–S30). The double crossovers in the newly attached DAE-E tile restricts the bending of the DNA helices and the distortions of the multimer. An energy cost is involved in this process.

Thermodynamic Measurement of Single DAE-E Tile Attachment. For thermodynamic measurement, one strand of the DAE-E tile was modified with TAMRA (acceptor). Another strand of the multimer was modified with 6-FAM (donor) (Figure 2G). Efficient Förster resonance energy transfer (FRET) only occurs when the 6-FAM-modified multimer and TAMRA-modified DAE-E tile assemble, which allows real-time observation of the attachment/detachment process with a quantitative polymerase chain reaction (qPCR) system. In a typical thermodynamic measurement, the fluorescence intensity of 6-FAM was recorded for two sets of replicated samples: one set was labeled with FRET donor (I_{donor}), the other one was labeled with both donor and acceptor ($I_{donor/acceptor}$). The donor-only sample contained the 6-FAM-modified multimer and the unmodified DAE-E tile, which accounted for the fluctuation of 6-FAM intensity with temperature change. The difference in intensity between I_{donor} and $I_{donor/acceptor}$ ($\Delta I = I_{donor} - I_{donor/acceptor}$) was calculated and normalized to obtain the fraction of attached tile (θ), which varies from 0 (high temperature) to 1 (low temperature) (details in the Supporting Information, section 1). The transition temperatures (T_m and

T_f) and widths (w) were identified by fitting the first derivative of θ versus temperature (T) with a Gaussian function. All scenarios showed reversible transitions with overlapping heating and cooling curves (Figures S9–S17); the T_m and T_f values for the same scenarios were within 0.4 °C (Tables S3–S8), which indicated that the samples reached equilibrium state at temperatures relevant to binding. The equilibrium constant (K_{eq}) was calculated from θ and the initial concentrations of the multimer and tile (C_0) assuming a two-state reaction. Standard enthalpy ($\Delta H°$) and entropy ($\Delta S°$) changes were obtained from the van't Hoff plot in the transition temperature range. Finally, the standard Gibbs free energy change ($\Delta G°$) at 25 °C for each scenario was calculated from $\Delta H°$ and $\Delta S°$. All of the thermodynamic parameters processed from FRET data are summarized in Tables S3–S9.

1b Binding of Two DX Monomers. The default 1b scenario involves monovalent binding (SE-1/1*) between two DAE-E tiles, which has a T_m below the lower temperature limit (25 °C) of the qPCR system used. Thus, the thermodynamic parameters for the series of 1b scenarios were measured using a fluorometer. The T_m of the default 1b scenario is 16.4 ± 0.4 °C, $\Delta G°_{1b}$ is −8.7 ± 0.1 kcal/mol. Since the experimental concentrations of the tiles are generally in the 10−100 nM range, the assembly yield is expected to be less than 20% at room temperature. Therefore, the tile dimers or trimers associated solely with one sticky end are quite labile at room temperature.

The standard binding free energy change of each individual pair of sticky ends ($\Delta G°_{SE}$) was measured by the UV thermal curves of hairpin pairs (Table S2). The $\Delta G°_{SE}$ of SE-1/1* without dye labeling was measured to be −10.1 ± 0.2 kcal/mol. The +1.4 kcal/mol difference between the fluorescence and UV thermal results may be attributed to the dye effect that destabilizes the pairing of sticky ends. The theoretical $\Delta G°_{SE,theor}$ calculated from the nearest-neighbor (NN) model[57–59] (including coaxial stacking base pairs flanking the sticky end) is approximately −8.4 kcal/mol for the same sequence. Since there is still uncertainty about the energy of dangles[60] and nicks[61] in the NN model, the sum of experimentally measured $\Delta G°_{SE}$ of the sticky ends involved in binding was used as the reference standard to compare with the measured free energy changes of the corresponding scenario ($\Delta G°$) (Figure 3C).

1b-L and 1b-S Binding between a DX Tile and a Prelinked Dimer. Besides default 1b, we studied two more 1b scenarios: 1b-L and 1b-S (illustrated as the unfavorable steps in Figure 1A). The 1b-L dimer carried a binding site without any neighboring tile, while the 1b-S dimer carried a binding site flanked by a neighboring tile. The 1b-S attachment ($T_m = 15.7$ ± 0.1 °C and $\Delta G° = −8.6 ± 0.1$ kcal/mol) was slightly less stable (<1.0 °C and ~0.1 kcal/mol) than the 1b-L and default 1b. Although the incoming tile in 1b-S was expected to experience more steric hindrance and electrostatic repulsion as compared to 1b and 1b-L, the slight difference between $\Delta G°_{1b-L}$ and $\Delta G°_{1b-S}$ suggests that when tiles are forced into sideway proximity in the product complex, the energy penalty is mostly relieved as long as the tile is not "locked" into the product by two or more bonds. The presence of nick points between individual DAE-E units within the multimer grants the 3D flexibility inherent in DNA tile assemblies, approaching energy minimum by some degree of structural distortions (*e.g.*, outward helical bending).

2b-S and 2b-L Binding of a DX Tile with Trimers. 2b-S and 2b-L scenarios showed significantly higher T_m and more

negative $\Delta G°$ compared to the 1b cases. Both scenarios have free energy changes significantly smaller than the sum of the two $\Delta G°_{SE}$ involved, which indicates that an energy penalty is present since the tetrameric product complex is constrained due to the formation of a closed "loop" (Loop4 penalty, $\Delta G°_{Loop4}$). The 2b-S attachment ($T_m = 41.7 ± 0.2$ °C, $\Delta G°_{2b-S} = −14.3 ± 0.3$ kcal/mol) is more stable than the 2b-L ($T_m = 35.1$ ± 0.1 °C, $\Delta G°_{2b-L} = −12.3 ± 0.1$ kcal/mol). SE-1 is shared by both scenarios, while SE-2 in 2b-S is stronger than SE-3 in 2b-L by a $\Delta\Delta G°$ of −1.6 kcal/mol (Table S2). The differences in thermostabilities (~2.0 kcal/mol) between 2b-S and 2b-L are largely accounted for by the different sequences of sticky ends, rather than the different geometrical arrangements of the sticky ends. Similar amount of energy penalty has to be overcome in both scenarios since the tetrameric product complexes (Loop4) are equally constrained.

3b and 4b Binding of a DX Tile with Multimers. With an increasing number of bonds formed, the T_ms of 3b and 4b are 44.0 ± 0.2 and 45.8 ± 0.1 °C, respectively. The corresponding trend of $\Delta G°$ is consistent with the trend of T_m, as more sticky end base pairings contribute to more stable binding, which requires a higher temperature to dissociate. For n-bond attachment ($n = 1–4$), the sum of $\Delta G°_{SE}$ and the experimentally measured binding free energies are linearly correlated with the number of bonds (Figure 3C). The difference between the sum of $\Delta G°_{SE}$ and the experimental $\Delta G°$ reflects the energy penalty, which is proportional to the number of bonds. Comparing the AFM images before and after tile binding, the interaction of the incoming tile with the flexible multimers requires a reconfiguration of both to adapt to a more rigid and compact conformation in the bound state (Figure 2H). During this process, more of the constrained Loop4s are formed for larger multimers carrying more sticky ends.

Despite the higher entropic penalties for 3b and 4b, the higher enthalpy gain determines the overall free energy favorability. However, theses types of attachment with more than two sticky ends are not considered to be primary contributors in the nucleation stage of tile-based assembly, although they may appear after cluster−cluster association.

Sources of Energy Penalty. The existence of energy penalty in the DNA tile assembly has been reported previously.[62] The enthalpy and entropy change of DNA nanotube polymerization has been quantified using total internal reflection fluorescence (TIRF) microscopy.[62] Ideally, DNA nanotube elongation involves only 2b-S attachment. The $\Delta H°$ and $\Delta S°$ were reported as −87.9 ± 2.0 kcal/mol and −0.252 ± 0.006 kcal/mol·K, respectively, for DAO-O tiles with 6-nt sticky ends;[62] so that the $\Delta G°$ at 25 °C is −12.8 ± 2.0 kcal/mol. If we only consider the sequence-dependent variation of the sticky ends by the NN model and take the reported free energy penalty for duplex hybridization initiation ($\Delta G°_{initiation} ≈ 1.90$ kcal/mol) into account,[58] the free energy change to attach a single tile through two 6-nt sticky ends to the end of a DNA nanotube can be calculated to be −18.9 kcal/mol (see Supporting Information, section 3 for details). The ~6 kcal/mol difference between the NN model calculation and the experimental result suggests that additional energy penalties exist, for example, structural distortion and intertile repulsions.[62]

The energy penalties have not been considered in the theoretical calculation, especially for the cases when constrained loops are formed. The tension of constrained loops is evidenced by the observation of a gap between the parallel

helices in DNA origami and tile arrays, which results in double-helix bending.[44,63]

To quantify the free energy change of formation (ΔG_f°) for an arbitrary tile complex ($\Delta G_{complex}^\circ$) and the loop penalty (ΔG_{Loopn}°, n denotes the number of tiles composing the loop), we made the following assumptions:

1. For any tile motif of interest, the sequence-dependence of the free energy change is primarily confined to the sticky end interactions.

2. Sealing nicks within the tile multimers has minimal effect on either thermodynamics or kinetics of the single tile attachment through sticky ends.

3. A loop penalty (ΔG_{Loopn}°) is defined as the energy penalty to attach a tile to form a constrained loop of n tiles. ΔG_{Loopn}° is sequence-independent and exclusively determined by the size of the loop (Figure 4B).

4. The ΔG_f° of the reactant complex ($\Delta G_{reactant}^\circ$) is defined as the sum of ΔG_{Loopn}°; if the reactant complex does not contain any closed loop, it is considered to be unconstrained, $\Delta G_{reactant}^\circ$ is set as 0 (Figure 4A).

5. The ΔG_f° of the product complex ($\Delta G_{product}^\circ$) is defined as the sum of ΔG_{SE}° of the newly formed bonds and ΔG_{Loopn}°.

6. The free energy change for a binding scenario is defined as the difference between the product complexes and the reactant complexes.

$$\Delta G_{binding}^\circ = \sum \Delta G_{product}^\circ - \sum \Delta G_{reactant}^\circ \quad (1)$$

The free energy change of a single tile attachment depends mainly on the identity of sticky ends (length and sequence) and the configuration of the complex. The loop penalty includes loop entropy, electrostatic repulsion and structural distortion to overcome when attaching a tile to form a closed loop. The loop penalty depends on the tile motif and it is probably smaller for shorter DX tile (e.g., 12 nm DAO-E tile)[10] than the longer ones (e.g., 14 nm DAE-E used here).

Based on the principle of thermodynamic equivalency, the formation of Loop4 via either of the two-step pathways, "1b-L and 2b-L" or "1b-S and 2b-S" (Figures 1A and S6), should have the same free energy change. The differences between the measured free energy changes of the 2b binding (ΔG_{2b-S}° and ΔG_{2b-L}°) and the sum of the two specific ΔG_{SE}° involved was attributed to ΔG_{Loop4}°, that is, $\Delta G_{Loop4}^\circ = \Delta G_{2b-S}^\circ - (\Delta G_{SE-1}^\circ + \Delta G_{SE-2}^\circ) = \Delta G_{2b-L}^\circ - (\Delta G_{SE-1}^\circ + \Delta G_{SE-3}^\circ)$. ΔG_{Loop4}° was quantified as $+4.8 \pm 0.1$ kcal/mol at 25 °C (Table S10). The dye effect was treated as a systematic error and corrected in the calculation. It is noted that the size of a loop is not limited to 4 tiles; larger loops of 6 or 8 tiles also exist in DNA tile-based self-assembly when errors of sticky end pairing occur or a tile is missing in the middle of a tile array.

Thermodynamic Measurement of a Single DAE-E Tile Embedded into an Encircled Octamer. To better understand the thermodynamic aspect of single tile attachment and to confirm the idea of the loop penalty, an octamer (Loop8) with a rigid 4b (R4b) central binding site was generated by adding an extra DAE-E subunit onto the flexible 4b multimer to encircle the binding site (Figure 2F). A series of octamers with fewer sticky ends at the central cavity were derived from this R4B structure by omitting 1−3 sticky ends (Figure 3A), while keeping the remaining sticky ends and coaxial stacking base pairs to accommodate the original DAE-E tile in the cavity. A similar fluorescent labeling strategy and thermodynamic ramps

were employed for studying these more rigid tile binding scenarios.

All the thermodynamic parameters calculated from the FRET data are summarized in Table S4 and plotted in Figure 3B,C (along with the flexible multimers for direct comparison). As additional bonds contribute to a more stable binding, all the rigid binding scenarios maintained the same trends of transition temperatures (T_m and T_f) and ΔG°. Compared to the flexible versions (1b-4b), the T_m of the rigid scenarios improved by ~1–5 °C for the R2b-S, R3b, and R4b but remained unchanged for R1b and R2b-L.

The encircled octamer provides a cavity with increased local crowdedness at the binding site (penalty) and simultaneously confines the movement of sticky ends (benefit). From a loop point of view, the R1b-R4b octamers ($\Delta G_{reactant}^\circ$) contain a Loop8 ($\Delta G_{Loop8}^\circ$). For R1b, R2b-L, and R2b-S, the Loop8 does not change before and after the attachment of a new tile, but for R3b and R4b, the Loop8 disappears after the tile attachment.

Independent Loop Model. The ILM (Figure 4) was proposed to explain the experimental free energies of scenarios
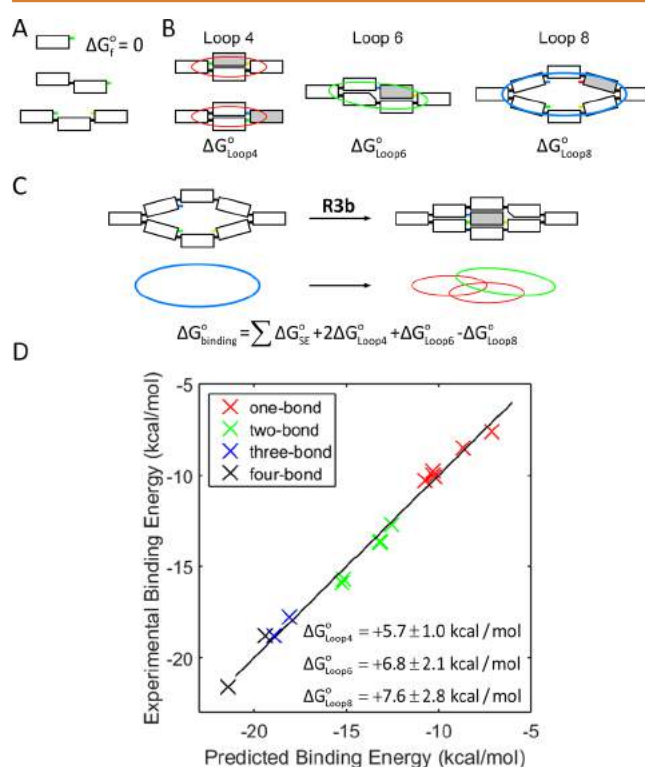

Figure 4. Independent loop model. (A) Free energy of formation of an arbitrary reactant is defined as 0 if it does not contain any closed loop. (B) Loop penalty is defined as the free energy loss to attach a tile (gray) to close a constrained loop. Loops of 4, 6, and 8 tiles are marked with red, green, blue circles, respectively. (C) Example scenario (R3b) of the linear combination of sticky end energy and the loop penalties. (D) Plot of experimental free energies vs predicted free energies of all the scenarios in this study.

by a linear combination of the ΔG_{SE}° and the sequence-independent loop penalties associated with the tile configurations (i.e., ΔG_{Loop4}°, ΔG_{Loop6}°, ΔG_{Loop8}°). The ILM assumes no interloop tension, that is, the formation of a new loop at the growth frontier does not affect the energy of pre-existing loops; therefore, the energy change of an arbitrary scenario is

decomposed into the sum of the ΔG_{SE}° and integeral multiples of loop penalties (Table S11):

$$\Delta G_{binding}^{\circ} = \sum \Delta G_{SE}^{\circ} + x\Delta G_{Loop4}^{\circ} + y\Delta G_{Loop6}^{\circ} + z\Delta G_{Loop8}^{\circ} \qquad (2)$$

where x, y, and z are integers that vary with the binding scenarios. A "least square" fit was used to derive ΔG_{Loop4}°, ΔG_{Loop6}°, and ΔG_{Loop8}° from the experimentally measured $\Delta G_{binding}^{\circ}$ and ΔG_{SE}° (Figure 4D). The ILM could fit the data by perturbing the ΔG_{SE}° by no more than 0.4 kcal/mol. The values of ΔG_{Loop4}°, ΔG_{Loop6}°, and ΔG_{Loop8}° were fitted to be +5.7 ± 1.0, +6.8 ± 2.1, and +7.6 ± 2.8 kcal/mol, respectively. The errors represent the fitting uncertainty.

To generalize the idea of loop penalties to DNA tile-based self-assembly, we used this idea to consider the energy penalty during the growth of a nanotube of DX tiles with n·tile circumference. A new Loop4 forms when a new tile attaches to the end of the nanotube. The average energy penalty for a single tile attachment at the growth stage of a DNA tube or lattice equals to ΔG_{Loop4}°. We experimentally measured the free energy change of a DNA nanotube in the growth stage (Figure S21). The ΔG_{Loop4}° was deduced from the difference between the sum of ΔG_{SE}° and the measured free energy change of tube growth. Assuming that tube growth is exclusively through 2b-S scenario, ΔG_{Loop4}° was calculated to be +3.1 ± 0.4 kcal/mol. The ΔG_{Loop4}° is expected to reduce when the binding site is on a tube growth frontier (Figure S20) because the frontier tiles have less flexibility than a 2b-S trimer which is present in the nucleation stage.

In addition to the previously revealed tile curvature,[64] curved tile connection[36] and the anisotropy of tile geometry,[65] the thermodynamics could also account for the formation of long ribbons or tubes of 2D DX tile arrays. The nonuniform affinities of the individual sticky ends favor the tile attachment along the diagonal axis of the stronger sticky end. During the cooling ramp of annealing, the stronger sticky ends associate earlier than the weaker sticky ends. The free tiles are preferentially consumed by the elongation of lattice along the axis with a larger free energy decrease.

Kinetic Measurements of Single DAE-E Tile Attachment. For the kinetic measurements, a 6-FAM was modified adjacent to a rationally designed sticky end (SE-1) on the multimers,[66] while the DAE-E tile was unmodified. The emission of 6-FAM was partially quenched by a guanine located in the single-stranded SE-1 by photoinduced electron transfer.[67−70] The hybridization of SE-1 by the DAE-E tile enhances the fluorescence intensity as the guanine is isolated from the 6-FAM. The fluorescence enhancement could be monitored isothermally over time immediately after mixing. The temperature ranges for the kinetic measurements were determined by the acquired thermodynamic parameters. The highest temperature for the kinetic measurements was chosen to be at least 15 °C below the corresponding T_m to ensure the dominance of the forward reaction in the fitting function. Thus, the temperature range was chosen from 12 to 20 °C with 2 °C intervals (or 12−21 °C with 3 °C intervals). The kinetic curves (6-FAM intensity vs time) were fitted with a second-order reaction model to obtain the rate constant (k, detailed fitting model in the Supporting Information, section 1). The rate constants were measured at 4−5 different temperatures (Figure 5 and Table S14) to obtain the activation energy (E_a) and pre-

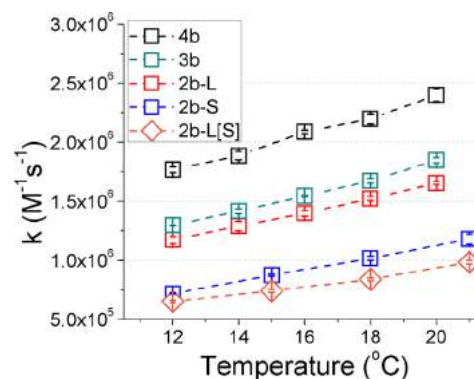exponential factor (A) from the Arrhenius plot (Figure S23 and Table S20).

Figure 5. Rate constants of different binding scenarios. More sticky ends contribute to the faster on-rate under isothermal conditions, which is dependent on nucleation accessibility. The dashed lines are guides for the eye.

Under the experimental conditions, the rate-limiting step is the "nucleation" of complementary sticky ends, which is a borrowed term that describes the correct recognition of a few base pairs (3−4-nt) to initiate the hybridization.[71−73] After successful "nucleation", a relatively rapid "zipping" step follows to accomplish the optimal base pairing and stacking. The binding rate is determined by the "nucleation" energy barrier, the accessibility of the binding site and the possibility of effective collision.[74,75]

The second-order rate constant k increases with the number of sticky ends as more bases are available for "nucleation". At 18 °C, the rate constant of 2b-L scenario ($1.52 \pm 0.02 \times 10^6$ M^{-1}·s^{-1}) is approximately 1.5-fold of 2b-S scenario ($1.02 \pm 0.01 \times 10^6$ M^{-1}·s^{-1}), although 2b-S is thermodynamically more stable. The rate constants of 3b and 4b were $1.67 \pm 0.02 \times 10^6$ and $2.20 \pm 0.04 \times 10^6$ M^{-1}·s^{-1} at 18 °C, respectively (Figure 5 and Table S14). More sticky ends contribute to better nucleation probability, but sticky ends with different sequences contribute differently. The improved nucleation probability is partially balanced out by a reduced accessibility to the binding site embedded in a bulkier multimer.

To rule out the sequence dependence of binding rates, we designed a "2b-L[S]" trimer by replacing SE-3 in the 2b-L trimer by SE-2. The resultant 2b-L[S] trimer carries not only the identical sticky ends as 2b-S trimer but also the identical coaxial stacking base pairs. This modification reduced k to $0.84 \pm 0.01 \times 10^6$ M^{-1}·s^{-1} at 18 °C (Figure 5). The 2b-S scenario is ~20% faster than 2b-L[S] when the same sticky ends are involved. The kinetics of tile attachment showed strong sequence dependence,[76] possibly due to the formation of secondary structures within the same sticky end or between neighboring sticky ends. Compared to the faster kinetics of DAE-E tile dimerization with two 5-nt sticky ends ($1.94 \pm 0.08 \times 10^6$ M^{-1}·s^{-1} at 18 °C),[66] two factors may result in the slower kinetics of the 2b-L and 2b-S attachments: the translational and rotational diffusion rates of the trimers are slower than a single DAE-E tile; moreover, the 2b-L and 2b-S attachments are more analogous to the semirigid dimerization scenario[66] regarding multimer flexibility.

Steric crowding effects could also affect kinetics. In 2b-S trimer, each sticky end is flanked by a 5-thymine sequence
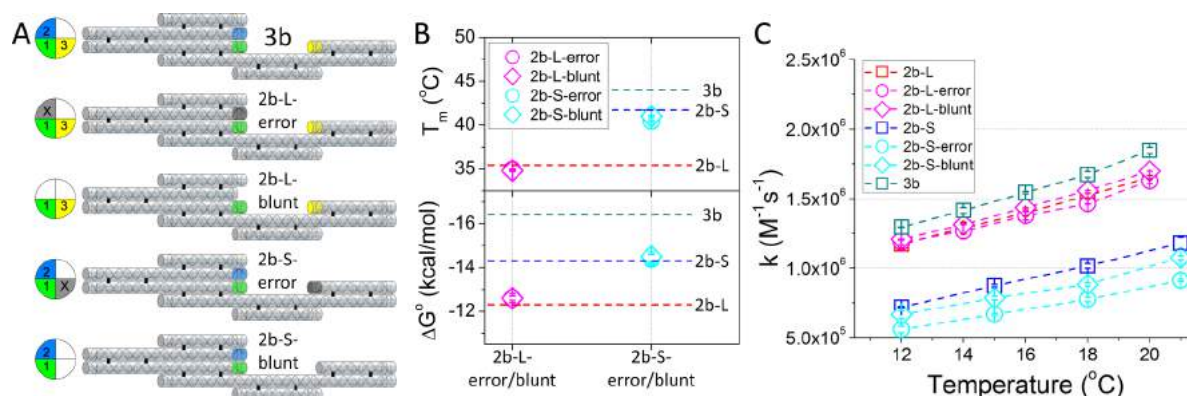
Figure 6. Thermodynamics and kinetics of tile attachment with error. (A) DNA helix model of the binding scenarios with perfect 3b, and the modified cases of the same 3b multimer with one incorrect sticky end (gray x) or a blunt end (one sticky end chopped off). (B) Comparison of the melting temperature (T_m) and standard free energy change ($\Delta G°$) of the binding scenarios shown in (A). The 3b, 2b-L, and 2b-S data are plotted as dashed lines for comparison. (C) Comparison of the rate constants of the binding scenarios shown in (A). The 3b, 2b-L, and 2b-S data are plotted for comparison.

extended from the neighboring helix that partially blocks the binding site. The 5-thymine sequences adjacent to the binding sites are lacking in the 2b-L trimer. We found that this subtle structural difference did affect the kinetics. In a control sample, when the two 5-thymine sequences were removed (2b-S-no 5T) (Figure S3), the rate constant of 2b-S increased, exceeding that of the 2b-L scenario in the original design and became 2-fold as fast as the 2b-L[S] (Tables S16 and S18). Removing these 5-thymine sequences not only eliminated any transient secondary structure, but also reduced steric hindrance at the binding site.

In the growth stage, the 2b-S attachment is expected to accelerate when the binding site is located on the growth frontier of a more rigid, extended lattice (in analogous to the rigid tile dimerization[66]), which benefits the possibility of successful "nucleation". In this case, the rate of 2b-S attachment may reach the upper limit of DAE-E tile dimerization (Figure S20). This kinetic difference may lead to distinct morphology of the final product (e.g., tubes or long narrow ribbons), which reveals the preference of 2b-S pathway over 2b-L.

The natural logarithms of the pre-exponential factor A and the activation energy E_a derived from the Arrhenius plots are similar for all the scenarios (in the ranges of 23.5−29.7 for ln A and 5.6−9.2 kcal/mol for E_a). The slowest 2b-S scenario is mostly determined by the highest E_a. It should be noted that 2b scenarios present A and E_a values comparable to that of a semirigid dimer comprising a DAE-E tile and Holliday junction.[66] With an increased flexibility, although the energy cost of distortion and bending of DNA helices to initiate binding is reduced, the probability of successful collision also decreases. The rate constant of tile binding reflects a consequence of sequence dependence, structural flexibility and the accessibility of the binding site.

Thermodynamics and Kinetics of Tile Attachment Through One Incorrect Bond. Errors may occur when tiles assemble, especially under highly supersaturated conditions. We constructed binding sites with a mismatched sticky end (error) to study how the thermostability and binding rates are affected by the error. One of the three sticky ends in the 3b multimer was replaced by 5-thymine (Figure 6A) to serve as a model scenario with an error (referred to as 2b-L-error and 2b-S-error). The 5-thymine error was then eliminated to serve as a blunt-end control (referred to as 2b-L-blunt and 2b-S-blunt).

The thermodynamic parameters of the erroneous scenarios and controls were plotted along with the above-mentioned 2b-L, 2b-S, and 3b for comparison (Figure 6B, data in Table S5). The error and blunt scenarios are significantly less stable than the 3b scenario, but they are comparable to the corresponding 2b scenarios (Figure 6B). The presence of a mismatched sticky end and two extra tile subunits in the modified multimer has minimal impact on the binding stability as long as the correct sticky ends remain the same. It is likely that the extra tile subunits bend away from the binding site and do not interact with tile attachment. The difference between $\Delta G°_{2b-L}$ and $\Delta G°_{2b-S}$ still holds for $\Delta G°_{2b-L-error}$ and $\Delta G°_{2b-S-error}$ (∼1.8 kcal/mol), which reflects the different total $\Delta G°_{SE}$ between the L and S scenarios.

The binding kinetics was examined over a temperature range from 12 to 20 °C (12 to 21 °C for the 2b-S scenarios). Compared to the 3b scenario, the binding rate decreases by 8 and 57% for 2b-L-error and 2b-S-error, respectively (Figure 6C). This is consistent with the fact that reducing the number of matching sticky ends reduces the binding rate by decreasing available nucleation site. Notably, the binding rates of 2b-S-error and 2b-S-blunt are 24 and 14% lower than that of 2b-S, possibly due to the presence of the extra subunits neighboring the binding site which reduces binding site accessibility. The binding rates of various 2b-L scenarios are similar. Despite the bulky 2b-L-error/blunt multimer, the subunit carrying the mismatched sticky end is repelled off and tilted away from the binding site as evidenced by the morphology of the 3b multimer before binding (Figure 2H), thus the exta subunits cause little steric hindrance. From these observations, we conclude that the primary determining factor for the slower binding rate of 2b-S compared to 2b-L is the sequence of the sticky ends. Another noticeable influencing factor is the steric crowding effects on the nucleation probability.

CONCLUSIONS

In summary, we used fluorescence-based technology to monitor different binding scenarios that could take place when DX tiles self-assemble into larger tile arrays and investigated their thermodynamic and kinetic properties. The independent loop model was proposed to account for the thermodynamics of all the scenarios studied, the model parameters of the ILM can be generalized to predict the energy of arbitrary tile configurations.

We found that differences in the thermostability of 2b-L and 2b-S scenarios can be well explained by the different sticky ends used; similar energy penalties are involved in both scenarios. Their remarkable differences in kinetics are also attributed to sequence dependence. However, stronger sticky ends do not necessarily lead to faster kinetics under the experimental conditions due to the tendency to form secondary structure among themselves. The binding rate of the weaker 2b-L scenario is almost 1.5-fold of 2b-S. The formation of ribbon or tube-like morphologies of 2D DX tile crystals can be both thermodynamically and kinetically determined, depending on the degree of nonuniformity of the individual sticky ends, the isothermal condition, or temperature ramp. One lesson we learned is that the sticky end binding energy cannot be accurately predicted from the current available NN model and they require individual experimental measurements. The binding thermodynamics and kinetics in some low probability or error-existing scenarios were also studied, and the conclusions support the above-mentioned findings. Two key assumptions of kTAM have been confirmed in this study, including that (1) the binding free energy is linearly correlated with the number of bonds and (2) mismatched sticky ends neither contribute to a significant energy benefit nor bring any energy penalty.

Some of our observations are different from the kTAM assumptions. Specifically, the binding free energy does not equal to the sum of each individual sticky ends involved; it is partially compromised by an energy penalty that accumulates with the number of constrained loop formation. The on-rate of tile attachment is not equivalent for all binding scenarios, it depends on the sequence identity of the sticky ends as well as the steric effects of the binding site. The results revealed here will be helpful for further refining the kTAM model by taking the different sources of energy penalty and kinetic parameters into consideration, so that we may improve future designs and simulations of tile-based self-assembly.

It should be noted that the geometries of assemblies using various DX tile motifs (DAE-E, DAE-O, DAO-O, *etc.*) are different. There are other factors that may affect both the thermodynamic and kinetics, such as sequence design (especially those base pairs that flanked the crossover points and sticky ends), nick point positioning, concentrations of monovalent and divalent cations used in the buffer solution. It is not absolutely critical to use junction sequences that are known to display preferred base-stacking in alignment with the orientation of the DNA helixes, but it is recommended to employ uniform sticky ends in the rational design of higher order tile-based assembly systems. One can also tune the sticky end sequences and/or lengths to differentiate thermostabilities of various binding scenario to favor hierarchical assembly that follows specific assembly route.[77]

METHODS

Self-Assembly of DNA Nanostructures. All the DNA strands were purchased from Integrated DNA Technologies (IDT). Unmodified and 6-FAM-modified oligos were purified by denaturing polyacrylamide gel electrophoresis (PAGE). TAMRA-modified oligos were purified by IDT using high-performance liquid chromatography (HPLC). Detailed DNA sequences and structural designs are shown in the Supporting Information. The concentrations of the strands were measured by absorbance at 260 nm in deionized water and calculated using the extinction coefficients provided by IDT. For each structure, equal molar amounts of DNA strands were mixed together at a final concentration of 500 nM in 1× TAE/Mg^{2+} buffer (Tris base 40 mM,

acetic acid 20 mM, EDTA·Na$_2$·12H$_2$O 2 mM, (CH$_3$COO)$_2$Mg·4H$_2$O 12.5 mM) and then annealed from 90 to 4 °C in about 12 h. The annealing procedure was as follows: the sample was first heated to 90 °C, then the temperature was reduced from 90 to 71 °C at 1 °C/5 min, from 70 to 41 °C at 1 °C/15 min, and from 40 to 26 °C at 1 °C/10 min. The temperature was held for 30 min at 25 °C then incubated at 4 °C until use. The annealing procedure was processed with an automated polymerase chain reaction (PCR) thermocycler (Mastercycler Pro, Eppendorf).

Thermodynamic Measurements. Fluorescence thermal curves were measured in optical tube strips using an Mx3005P quantitative PCR system (Agilent Technologies), which is a real-time thermocycler equipped with a fluorescent 96-well plate reader. The DNA strands were mixed in equimolar amounts at final concentrations of 100 nM in 1× TAE/Mg^{2+} buffer. The DAE-E tile was modified with TAMRA (FRET acceptor), and the multimer were modified with 6-FAM (FRET donor). When binding occurs, the two dyes come closer and FRET is monitored. The mixtures of the strands (30 μL) containing only the donor (the strand labeled with TAMRA was replaced with an unlabeled strand of the same sequence) or both the donor and acceptor were pipetted in the optical tubes, covered with optical transparent caps, and placed in the thermocycler. The fluorescence intensity of 6-FAM emission was monitored at 522 nm with excitation at 495 nm at 1 min intervals throughout the thermal program. The samples were first heated to 80 °C for 5 min, and the temperature was reduced from 80 to 25 °C at −0.1 °C/min. After cooling to 25 °C, the samples were held for 10 min and then heated to 80 °C at +0.1 °C/min. The scenarios of one sticky end attachment (1b) have a T_m below the 25 °C temperature limit of the qPCR system; thus, the thermodynamic parameters for the 1b scenarios were measured using Nanolog fluorometer (Horiba Jobin Yvon) equipped with a temperature-controlled sample holder linked to a refrigerated water bath circulator (Thermo Scientific, NESLAB RTE 7). The fluorescence thermal curves of "donor only" and "donor/acceptor" mixtures (100 nM) were measured by gradually increasing the temperature from 12 to 25 °C (+0.1 °C/min). The fluorescence intensity of 6-FAM emission was monitored at 520 nm (emission slit width 5 nm) with excitation at 497 nm (excitation slit width 1 nm) at 10 min (*i.e.*, 1.0 °C) intervals. The UV thermal curves were measured in quartz cuvettes (Starna Cells) using a CARY 300BIO UV−vis spectrometer with temperature control accessories. The pair of DNA strands were mixed in equimolar amounts at final concentrations of 2 μM in 1× TAE/Mg^{2+} buffer. The concentrations of DNA strands used in the UV thermal measurements were 20-fold higher than the concentration used for fluorescence thermal measurements (100 nM). This difference will affect the T_m values significantly, but the free energy changes calculated from the van't Hoff plot should be concentration-independent. The mixtures of the strands (135 μL) were pipetted in the cuvettes, and 300 μL of mineral oil was layered on top of the strand mixture to prevent sample evaporation during the temperature ramps. The UV absorbance of DNA at 260 nm (A260) was recorded at 1 min intervals throughout the thermal program. A 1× TAE/Mg^{2+} buffer was used as the background reference. The samples were first heated to 90 °C for 5 min, and the temperature was reduced from 90 to 15 °C at −0.1 °C/min. After cooling to 15 °C, the samples were held for 10 min and then heated to 65 °C at +0.1 °C/min. The cycling between 65 and 15 °C showed perfect reversibility.

Kinetic Measurements. The fluorescence change over reaction time was monitored with a Nanolog fluorometer (Horiba Jobin Yvon). To ensure the accuracy of the kinetics test, sample injection was performed with a stopped flow accessory (SFA-20, TgK Scientific) that can mix equal volumes of two samples and inject the mixtures into a cuvette for fluorescence recording in about 0.01 s (a nominal dead time <8 ms according to manufacturer's specifications). In a typical experiment, 60 μL each of the tile and multimer solutions (final concentrations of 10 nM for both species) was used for all kinetic measurements. The parameters settings of the fluorescence measurements were as follows: 497 nm excitation, 1 nm excitation slit, 520 nm emission, 15 nm emission slit. The excitation slit is minimized to reduce exposure of the samples to the excitation light and thus prevent

photobleaching of the dye molecules (especially at such low concentrations). The emission slit was 15 nm wide to improve the emission light intensity (signal level). The detector was cooled to minimize noise. The signal was collected from 0 to 300 s with 0.5 s integration time and 1 s intervals. Binding kinetics measurements were repeated 4−6 times at each temperature and recorded at 4−5 different temperatures. The maximum temperature of each binding scenario was at least 15 °C below the melting temperature to ensure that the rate of the forward reaction (association) far exceeds that of the backward reaction (dissociation). The rate constant of the reaction was obtained by fitting the data as described in the Supporting Information.

ASSOCIATED CONTENT

ⓈSupporting Information

The Supporting Information is available free of charge on the ACS Publications website at DOI: 10.1021/acsnano.7b04845.

> Data analysis, DNA structure design and sequences, gel electrophoresis images, additional fluorescence and UV thermal profiles, kinetic data, and additional AFM images (PDF)

AUTHOR INFORMATION

Corresponding Authors
*E-mail: hao.yan@asu.edu.
*E-mail: yan_liu@asu.edu.
ORCID
Shuoxing Jiang: 0000-0002-9235-6447
Fan Hong: 0000-0002-3370-7833
Huiyu Hu: 0000-0002-6936-2398
Hao Yan: 0000-0001-7397-9852
Yan Liu: 0000-0003-0906-2606

Author Contributions
[†]S.J. and F.H. contributed equally to this work. S.J., H.Y., and Y.L. designed the study; S.J., F.H., and H.H. performed the research; S.J. and F.H. analyzed data.

Notes
The authors declare no competing financial interest.

ACKNOWLEDGMENTS

REFERENCES

(1) Seeman, N. C. DNA Nanotechnology: Novel DNA Constructions. *Annu. Rev. Biophys. Biomol. Struct.* **1998**, *27*, 225−248.
(2) Pinheiro, A. V.; Han, D.; Shih, W. M.; Yan, H. Challenges and Opportunities for Structural DNA Nanotechnology. *Nat. Nanotechnol.* **2011**, *6*, 763−772.
(3) Zhang, F.; Nangreave, J.; Liu, Y.; Yan, H. Structural DNA Nanotechnology: State of the Art and Future Perspective. *J. Am. Chem. Soc.* **2014**, *136*, 11198−11211.
(4) Chen, Y.-J.; Groves, B.; Muscat, R. A.; Seelig, G. DNA Nanotechnology From the Test Tube to the Cell. *Nat. Nanotechnol.* **2015**, *10*, 748−760.
(5) Seeman, N. C. An Overview of Structural DNA Nanotechnology. *Mol. Biotechnol.* **2007**, *37*, 246−257.
(6) Modi, S.; Bhatia, D.; Simmel, F. C.; Krishnan, Y. Structural DNA Nanotechnology: From Bases to Bricks, From Structure to Function. *J. Phys. Chem. Lett.* **2010**, *1*, 1994−2005.

(7) Lin, C.; Liu, Y.; Rinker, S.; Yan, H. DNA Tile Based Self-Assembly: Building Complex Nanoarchitectures. *ChemPhysChem* **2006**, *7*, 1641−1647.
(8) Mao, C.; Sun, W.; Seeman, N. C. Designed Two-Dimensional DNA Holliday Junction Arrays Visualized by Atomic Force Microscopy. *J. Am. Chem. Soc.* **1999**, *121*, 5437−5443.
(9) Malo, J.; Mitchell, J. C.; Vénien-Bryan, C.; Harris, J. R.; Wille, H.; Sherratt, D. J.; Turberfield, A. J. Engineering A 2D Protein-DNA Crystal. *Angew. Chem., Int. Ed.* **2005**, *44*, 3057−3061.
(10) Winfree, E.; Liu, F.; Wenzler, L. A.; Seeman, N. C. Design and Self-Assembly of Two-Dimensional DNA Crystals. *Nature* **1998**, *394*, 539−544.
(11) Reishus, D.; Shaw, B.; Brun, Y.; Chelyapov, N.; Adleman, L. Self-Assembly of DNA Double-Double Crossover Complexes into High-Density, Doubly Connected, Planar Structures. *J. Am. Chem. Soc.* **2005**, *127*, 17590−17591.
(12) Zhang, X.; Yan, H.; Shen, Z.; Seeman, N. C. Paranemic Cohesion of Topologically-Closed DNA Molecules. *J. Am. Chem. Soc.* **2002**, *124*, 12940−12941.
(13) Shen, Z.; Yan, H.; Wang, T.; Seeman, N. C. Paranemic Crossover DNA: A Generalized Holliday Structure with Applications in Nanotechnology. *J. Am. Chem. Soc.* **2004**, *126*, 1666−1674.
(14) He, Y.; Chen, Y.; Liu, H.; Ribbe, A. E.; Mao, C. Self-Assembly of Hexagonal DNA Two-Dimensional (2D) Arrays. *J. Am. Chem. Soc.* **2005**, *127*, 12202−12203.
(15) He, Y.; Tian, Y.; Ribbe, A. E.; Mao, C. Highly Connected Two-Dimensional Crystals of DNA Six-Point-Stars. *J. Am. Chem. Soc.* **2006**, *128*, 15978−15979.
(16) He, Y.; Ye, T.; Su, M.; Zhang, C.; Ribbe, A. E.; Jiang, W.; Mao, C. Hierarchical Self-Assembly of DNA into Symmetric Supramolecular Polyhedra. *Nature* **2008**, *452*, 198−201.
(17) Zhang, F.; Liu, Y.; Yan, H. Complex Archimedean Tiling Self-Assembled From DNA Nanostructures. *J. Am. Chem. Soc.* **2013**, *135*, 7458−7461.
(18) Zhang, F.; Jiang, S.; Li, W.; Hunt, A.; Liu, Y.; Yan, H. Self-Assembly of Complex DNA Tessellations by Using Low-Symmetry Multi-Arm DNA Tiles. *Angew. Chem.* **2016**, *128*, 9006−9009.
(19) Ke, Y.; Ong, L. L.; Shih, W. M.; Yin, P. Three-Dimensional Structures Self-Assembled From DNA Bricks. *Science* **2012**, *338*, 1177−1183.
(20) Wei, B.; Dai, M.; Yin, P. Complex Shapes Self-Assembled From Single-Stranded DNA Tiles. *Nature* **2012**, *485*, 623−626.
(21) Ke, Y.; Ong, L. L.; Sun, W.; Song, J.; Dong, M.; Shih, W. M.; Yin, P. DNA Brick Crystals with Prescribed Depths. *Nat. Chem.* **2014**, *6*, 994−1002.
(22) Sha, R.; Liu, F.; Millar, D. P.; Seeman, N. C. Atomic Force Microscopy of Parallel DNA Branched Junction Arrays. *Chem. Biol.* **2000**, *7*, 743−751.
(23) Liu, D.; Wang, M.; Deng, Z.; Walulu, R.; Mao, C. Tensegrity: Construction of Rigid DNA Triangles with Flexible Four-Arm DNA Junctions. *J. Am. Chem. Soc.* **2004**, *126*, 2324−2325.
(24) Constantinou, P. E.; Wang, T.; Kopatsch, J.; Israel, L. B.; Zhang, X.; Ding, B.; Sherman, W. B.; Wang, X.; Zheng, J.; Sha, R.; Seeman, N. C. Double Cohesion in Structural DNA Nanotechnology. *Org. Biomol. Chem.* **2006**, *4*, 3414−3419.
(25) Hamada, S.; Murata, S. Substrate-Assisted Assembly of Interconnected Single-Duplex DNA Nanostructures. *Angew. Chem.* **2009**, *121*, 6952−6955.
(26) Sharma, J.; Ke, Y.; Lin, C.; Chhabra, R.; Wang, Q.; Nangreave, J.; Liu, Y.; Yan, H. DNA-Tile-Directed Self-Assembly of Quantum Dots into Two-Dimensional Nanopatterns. *Angew. Chem., Int. Ed.* **2008**, *47*, 5157−5159.
(27) Sharma, J.; Chhabra, R.; Cheng, A.; Brownell, J.; Liu, Y.; Yan, H. Control of Self-Assembly of DNA Tubules Through Integration of Gold Nanoparticles. *Science* **2009**, *323*, 112−116.
(28) Wilner, O. I.; Weizmann, Y.; Gill, R.; Lioubashevski, O.; Freeman, R.; Willner, I. Enzyme Cascades Activated on Topologically Programmed DNA Scaffolds. *Nat. Nanotechnol.* **2009**, *4*, 249−254.

(29) Fu, T. J.; Seeman, N. C. DNA Double-Crossover Molecules. *Biochemistry* **1993**, *32*, 3211−3220.

(30) Sa-Ardyen, P.; Vologodskii, A. V.; Seeman, N. C. The Flexibility of DNA Double Crossover Molecules. *Biophys. J.* **2003**, *84*, 3829−3837.

(31) Evans, C. G.; Winfree, E. *DNA Sticky End Design and Assignment for Robust Algorithmic Self-Assembly*, DNA Computing and Molecular Programming, LNCS 8141; Springer International Publishing: Cham, 2013; pp 61−75.

(32) Schulman, R.; Winfree, E. Synthesis of Crystals with A Programmable Kinetic Barrier to Nucleation. *Proc. Natl. Acad. Sci. U. S. A.* **2007**, *104*, 15236−15241.

(33) Evans, C. G.; Hariadi, R. F.; Winfree, E. Direct Atomic Force Microscopy Observation of DNA Tile Crystal Growth at the Single-Molecule Level. *J. Am. Chem. Soc.* **2012**, *134*, 10485−10492.

(34) Schulman, R.; Winfree, E. Programmable Control of Nucleation for Algorithmic Self-Assembly. *SIAM J. Comput.* **2010**, *39*, 1581−1616.

(35) Li, W.; Yang, Y.; Jiang, S.; Yan, H.; Liu, Y. Controlled Nucleation and Growth of DNA Tile Arrays within Prescribed DNA Origami Frames and Their Dynamics. *J. Am. Chem. Soc.* **2014**, *136*, 3724−3727.

(36) Rothemund, P. W.; Ekani-Nkodo, A.; Papadakis, N.; Kumar, A.; Fygenson, D. K.; Winfree, E. Design and Characterization of Programmable DNA Nanotubes. *J. Am. Chem. Soc.* **2004**, *126*, 16344−16352.

(37) Zhang, D. Y.; Hariadi, R. F.; Choi, H. M.; Winfree, E. Integrating DNA Strand-Displacement Circuitry with DNA Tile Self-Assembly. *Nat. Commun.* **2013**, *4*, 1965.

(38) Winfree, E. Algorithmic Self-Assembly of DNA. Ph.D. Thesis, California Institute of Technology, Pasadena, CA, 1998.

(39) Winfree, E. Algorithmic Self-Assembly of DNA: Theoretical Motivations and 2D Assembly Experiments. *J. Biomol. Struct. Dyn.* **2000**, *17*, 263−270.

(40) Fujibayashi, K.; Hariadi, R.; Park, S. H.; Winfree, E.; Murata, S. Toward Reliable Algorithmic Self-Assembly of DNA Tiles: A Fixed-Width Cellular Automaton Pattern. *Nano Lett.* **2008**, *8*, 1791−1797.

(41) Rothemund, P. W.; Papadakis, N.; Winfree, E. Algorithmic Self-Assembly of DNA Sierpinski Triangles. *PLoS Biol.* **2004**, *2*, e424.

(42) Wang, T.; Sha, R.; Dreyfus, R.; Leunissen, M. E.; Maass, C.; Pine, D. J.; Chaikin, P. M.; Seeman, N. C. Self-Replication of Information-Bearing Nanoscale Patterns. *Nature* **2011**, *478*, 225−228.

(43) Schulman, R.; Yurke, B.; Winfree, E. Robust Self-Replication of Combinatorial Information via Crystal Growth and Scission. *Proc. Natl. Acad. Sci. U. S. A.* **2012**, *109*, 6405−6410.

(44) Barish, R. D.; Schulman, R.; Rothemund, P. W.; Winfree, E. An Information-Bearing Seed for Nucleating Algorithmic Self-Assembly. *Proc. Natl. Acad. Sci. U. S. A.* **2009**, *106*, 6054−6059.

(45) Winfree, E. *Simulations of Computing by Self-Assembly*, CS-TR: 1988.22; California Institute of Technology: Pasadena, CA, 1988.

(46) Fujibayashi, K.; Murata, S. Precise Simulation Model for DNA Tile Self-Assembly. *IEEE Trans. Nanotechnol.* **2009**, *8*, 361−368.

(47) Pastré, D.; Hamon, L.; Landousy, F.; Sorel, I.; David, M.-O.; Zozime, A.; Le Cam, E.; Piétrement, O. Anionic Polyelectrolyte Adsorption on Mica Mediated by Multivalent Cations: A Solution to DNA Imaging by Atomic Force Microscopy Under High Ionic Strengths. *Langmuir* **2006**, *22*, 6651−6660.

(48) Woo, S.; Rothemund, P. W. Self-Assembly of Two-Dimensional DNA Origami Lattices Using Cation-Controlled Surface Diffusion. *Nat. Commun.* **2014**, *5*, 4889.

(49) Ercolani, G. Assessment of Cooperativity in Self-Assembly. *J. Am. Chem. Soc.* **2003**, *125*, 16097−16103.

(50) Seeman, N. C.; Kallenbach, N. R. Design of Immobile Nucleic Acid Junctions. *Biophys. J.* **1983**, *44*, 201−209.

(51) Miick, S. M.; Fee, R. S.; Millar, D. P.; Chazin, W. J. Crossover Isomer Bias is the Primary Sequence-Dependent Property of Immobilized Holliday Junctions. *Proc. Natl. Acad. Sci. U. S. A.* **1997**, *94*, 9080−9084.

(52) Li, X.; Wang, H.; Seeman, N. C. Direct Evidence for Holliday Junction Crossover Isomerization. *Biochemistry* **1997**, *36*, 4240−4247.

(53) McKinney, S. A.; Déclais, A.-C.; Lilley, D. M.; Ha, T. Structural Dynamics of Individual Holliday Junctions. *Nat. Struct. Biol.* **2003**, *10*, 93−97.

(54) Doye, J. P.; Ouldridge, T. E.; Louis, A. A.; Romano, F.; Šulc, P.; Matek, C.; Snodin, B. E.; Rovigatti, L.; Schreck, J. S.; Harrison, R. M.; Smith, W. P. J. Coarse-Graining DNA for Simulations of DNA Nanotechnology. *Phys. Chem. Chem. Phys.* **2013**, *15*, 20395−20414.

(55) Range, K.; Mayaan, E.; Maher, L., III; York, D. M. The Contribution of Phosphate-Phosphate Repulsions to the Free Energy of DNA Bending. *Nucleic Acids Res.* **2005**, *33*, 1257−1268.

(56) Maiti, P. K.; Pascal, T. A.; Vaidehi, N.; Goddard, W. A., III The Stability of Seeman JX DNA Topoisomers of Paranemic Crossover (PX) Molecules as A Function of Crossover Number. *Nucleic Acids Res.* **2004**, *32*, 6047−6056.

(57) SantaLucia, J. A Unified View of Polymer, Dumbbell, and Oligonucleotide DNA Nearest-Neighbor Thermodynamics. *Proc. Natl. Acad. Sci. U. S. A.* **1998**, *95*, 1460−1465.

(58) SantaLucia, J., Jr; Hicks, D. The Thermodynamics of DNA Structural Motifs. *Annu. Rev. Biophys. Biomol. Struct.* **2004**, *33*, 415−440.

(59) Protozanova, E.; Yakovchuk, P.; Frank-Kamenetskii, M. D. Stacked-Unstacked Equilibrium at the Nick Site of DNA. *J. Mol. Biol.* **2004**, *342*, 775−785.

(60) Bommarito, S.; Peyret, N.; Jr, S. Thermodynamic Parameters for DNA Sequences with Dangling Ends. *Nucleic Acids Res.* **2000**, *28*, 1929−1934.

(61) Yakovchuk, P.; Protozanova, E.; Frank-Kamenetskii, M. D. Base-Stacking and Base-Pairing Contributions Into Thermal Stability of the DNA Double Helix. *Nucleic Acids Res.* **2006**, *34*, 564−574.

(62) Hariadi, R. F.; Yurke, B.; Winfree, E. Thermodynamics and Kinetics of DNA Nanotube Polymerization From Single-Filament Measurements. *Chem. Sci.* **2015**, *6*, 2252−2267.

(63) Fischer, S.; Hartl, C.; Frank, K.; Radler, J. O.; Liedl, T.; Nickel, B. Shape and Interhelical Spacing of DNA Origami Nanostructures Studied by Small-Angle X-ray Scattering. *Nano Lett.* **2016**, *16*, 4282−4287.

(64) Kim, S.; Kim, J.; Qian, P.; Shin, J.; Amin, R.; Ahn, S. J.; LaBean, T. H.; Kim, M. K.; Park, S. H. Intrinsic DNA Curvature of Double-Crossover Tiles. *Nanotechnology* **2011**, *22*, 245706.

(65) Ke, Y.; Liu, Y.; Zhang, J.; Yan, H. A Study of DNA Tube Formation Mechanisms Using 4-, 8-, and 12-Helix DNA Nanostructures. *J. Am. Chem. Soc.* **2006**, *128*, 4414−4421.

(66) Jiang, S.; Yan, H.; Liu, Y. Kinetics of DNA Tile Dimerization. *ACS Nano* **2014**, *8*, 5826−5832.

(67) Marras, S. A.; Kramer, F. R.; Tyagi, S. Efficiencies of Fluorescence Resonance Energy Transfer and Contact-Mediated Quenching in Oligonucleotide Probes. *Nucleic Acids Res.* **2002**, *30*, 122e.

(68) Seidel, C. A.; Schulz, A.; Sauer, M. H. Nucleobase-Specific Quenching of Fluorescent Dyes. 1. Nucleobase One-Electron Redox Potentials and Their Correlation with Static and Dynamic Quenching Efficiencies. *J. Phys. Chem.* **1996**, *100*, 5541−5553.

(69) Kelley, S. O.; Barton, J. K. Electron Transfer Between Bases in Double Helical DNA. *Science* **1999**, *283*, 375−381.

(70) Nazarenko, I.; Pires, R.; Lowe, B.; Obaidy, M.; Rashtchian, A. Effect of Primary and Secondary Structure of Oligodeoxyribonucleotides on the Fluorescent Properties of Conjugated Dyes. *Nucleic Acids Res.* **2002**, *30*, 2089−2195.

(71) Pinheiro, A. V.; Nangreave, J.; Jiang, S.; Yan, H.; Liu, Y. Steric Crowding and the Kinetics of DNA Hybridization within A DNA Nanostructure System. *ACS Nano* **2012**, *6*, 5521−5530.

(72) Craig, M. E.; Crothers, D. M.; Doty, P. Relaxation Kinetics of Dimer Formation by Self Complementary Oligonucleotides. *J. Mol. Biol.* **1971**, *62*, 383−401.

(73) Ouldridge, T. E.; Šulc, P.; Romano, F.; Doye, J. P.; Louis, A. A. DNA Hybridization Kinetics: Zippering, Internal Displacement and Sequence Dependence. *Nucleic Acids Res.* **2013**, *41*, 8886−8895.

(74) Wetmur, J. G.; Davidson, N. Kinetics of Renaturation of DNA. *J. Mol. Biol.* **1968**, *31*, 349−370.

(75) Wetmur, J. G. Hybridization and Renaturation Kinetics of Nucleic Acids. *Annu. Rev. Biophys. Bioeng.* **1976**, *5*, 337−361.

(76) Zhang, J. X.; Fang, J. Z.; Duan, W.; Wu, L.; Zhang, A.; Dalchau, N.; Yordanov, B.; Petersen, R.; Phillips, A.; Zhang, D. Predicting DNA Hybridization Kinetics From Sequence. *bioRxiv* **2017**, 149427.

(77) Tikhomirov, G.; Petersen, P.; Qian, L. Programmable Disorder in Random DNA Tilings. *Nat. Nanotechnol.* **2016**, *12*, 251−259.